Hybrid shear force feedback/scanning quantitative phase microscopy applied to subsurface imaging

Kert Edward[1*], Faramarz Farahi[1] and Robert Hocken[2]

[1]*Department of Physics and Optical Science, University of North Carolina at Charlotte, Charlotte, NC, 28223, USA*
[2]*Center for Precision Metrology, University of North Carolina at Charlotte, Charlotte, NC, 28223, USA*
**kedward@uncc.edu*

Abstract: Quantitative phase microscopy allows for the study of the surface morphology and dynamics of transparent biological specimens. Although phase data often contains coupled subsurface information, decoupling the surface and subsurface components is often very difficult or impossible. We hereby present a simple procedure which exploits simultaneous obtained quantitative phase and shear-force feedback topography data to extract subsurface sample information. Our results reveal subsurface features in fabricated samples and fish erythrocytes.

OCIS codes: (180.5810) Scanning microscopy; (170.6900) Three-dimensional microscopy; (110.4190) Multiple imaging; (100.3175) Interferometric imaging; (170.1530) Cell analysis; (120.5050) Phase measurement; (100.2960) Image analysis.

References and links

1. O. W. Richards, "Phase microscopy 1950-1954," Science **120**(3121), 631–639 (1954).
2. F. Zernike, "How I discovered phase contrast," Science **121**(3141), 345–349 (1955).
3. M. Pluta, "Nomarski's DIC microscopy: a review," Proc. SPIE **1846**, 10–25 (1994).
4. X. Li, T. Yamauchi, H. Iwai, Y. Yamashita, H. Zhang, and T. Hiruma, "Full-field quantitative phase imaging by white-light interferometry with active phase stabilization and its application to biological samples," Opt. Lett. **31**(12), 1830–1832 (2006).
5. G. Popescu, L. P. Deflores, J. C. Vaughan, K. Badizadegan, H. Iwai, R. R. Dasari, and M. S. Feld, "Fourier phase microscopy for investigation of biological structures and dynamics," Opt. Lett. **29**(21), 2503–2505 (2004).
6. N. Lue, W. Choi, G. Popescu, T. Ikeda, R. R. Dasari, K. Badizadegan, and M. S. Feld, "Quantitative phase imaging of live cells using fast Fourier phase microscopy," Appl. Opt. **46**(10), 1836–1842 (2007).
7. W. S. Rockward, A. L. Thomas, B. Zhao, and C. A. Dimarzio, "Quantitative phase measurements using optical quadrature microscopy," Appl. Opt. **47**(10), 1684–1696 (2008).
8. H. W. Wolberg, W. N. Street, O. L. Mangasarian, "Importance of Nuclear Morphology in Breast," Cancer Prognosis Clin. Cancer Res. **5**, 3542–3548 (1999).
9. N. Lue, G. Popescu, T. Ikeda, R. R. Dasari, K. Badizadegan, and M. S. Feld, "Live cell refractometry using microfluidic devices," Opt. Lett. **31**(18), 2759–2761 (2006).
10. B. Rappaz, P. Marquet, E. Cuche, Y. Emery, C. Depeursinge, and P. Magistretti, "Measurement of the integral refractive index and dynamic cell morphometry of living cells with digital holographic microscopy," Opt. Express **13**(23), 9361–9373 (2005), http://www.opticsinfobase.org/abstract.cfm?&uri=oe-13-23-9361.
11. R. E. Marquis, "Immersion refractometry of isolated bacterial cell walls," J. Bacteriol. **116**(3), 1273–1279 (1973).
12. L. K. Chin, C. S. Lim, P. H. Yap, J. H. Ng, J. Z. Hao, S. Takahashi, and A. Q. Liu, "Single Living Cell Refractometry using FBG-Based Resonant Cavity," Solid-State Sensors, Actuators and Microsystems Conference, 2007. Transducers 2007. International 10–14 June 2007, pp. 851–854.
13. J. Lai, Z. Li, C. Wang, and A. He, "Experimental measurement of the refractive index of biological tissues by total internal reflection," Appl. Opt. **44**(10), 1845–1849 (2005).
14. K. Edward, T. W. Mayes, B. Hocken, and F. Farahi, "Trimodal imaging system capable of quantitative phase imaging without 2 π ambiguities," Opt. Lett. **33**(3), 216–218 (2008).
15. M. Servin, J. L. Marroquin, D. Malacara, and F. J. Cuevas, "Phase unwrapping with a regularized phase-tracking system," Appl. Opt. **37**(10), 1917–1923 (1998).
16. L. Zhang, Y. Zhang, C. Zhang, Y. Zhao, and X. Liu, "Terahertz multiwavelength phase imaging without 2π ambiguity," Opt. Lett. **31**(24), 3668–3670 (2006).
17. C. Polhemus, "Two-wavelength interferometry," Appl. Opt. **12**(9), 2071–2074 (1973).
18. F. de Lange, A. Cambi, R. Huijbens, B. de Bakker, W. Rensen, M. Garcia-Parajo, N. van Hulst, and C. G. Figdor, "Cell biology beyond the diffraction limit: near-field scanning optical microscopy," J. Cell Sci. **114**(Pt 23), 4153–4160 (2001).

#112155 - $15.00 USD Received 1 Jun 2009; revised 20 Jul 2009; accepted 11 Aug 2009; published 28 Sep 2009

19. K. Karrai, and R. D. Grober, "Piezoelectric tip-sample distance control for near field optical microscopes," Appl. Phys. Lett. **77**, 4272–4276 (2000).
20. E. H. W. Meijering, K. J. Zuiderveld, and M. A. Viergever, "Image registration for digital subtraction angiography," Int. J. Comput. Vis. **31**(2/3), 227–246 (1999).
21. M. Najiah, M. Dahirah, H. Marina, S. W. Lee, and W. H. Nazaha, "Quantitative comparisons of erythrocyte morphology in healthy freshwater fish species from Malaysia," Research J. Fisheries and Hydrobio. **3**, 32–35 (2008).

1. Introduction

Translucent samples such as biological cells lack sufficient intrinsic intensity modulation inducing features such as cell pigments, and as such are difficult to image using conventional optical microscopy techniques. A simple solution to this problem involves staining the sample with an appropriate dye. Although this procedure greatly improves the optical contrast, the dye often has a deleterious effect on the specimen sample. Phase contrast techniques such as those employed in Zernike's phase contrast microscope and the differential interference contrast microscope allow biological samples to be imaged by exploiting the endogenous contrast properties of sample thickness and refractive index [1–3]. Significant contrast is achieved but the result is qualitative in nature. Recently, several novel quantitative phase imaging techniques have been proposed and applied to the study of the surface morphology of biological specimens including red blood cells (RBCs) [4–7]. Erythrocytes are commonly used in quantitative phase investigations because depending on the species of origin, these simple cells are typically enucleated and can be considered to be homogenous. However, most biological cells are nucleated and contain several other subsurface organelles. Thus the resulting phase data contains valuable subsurface information which up until now has been ignored. Intracellular information such as the size, shape, volume and surface roughness of organelles such as the nucleus provide critical information which has been shown to be useful in breast cancer prognosis for example [8]. A significant hindrance to the utilization of phase information for subsurface studies is the separation of the coupled surface information in the resultant phase data. In recent research, it has been demonstrated that sample thickness and integrated refractive index contributions can be decoupled if the biological specimen is physically constraint, such as in a microfluidic chamber of known dimensions [9]. Another interesting procedure for decoupling cell thickness/ refractive index information involves utilizing phase measurements obtained subsequent to immersion of the investigated sample in two different liquid mediums with slightly different refractive indices [10]. Several other techniques have been investigated [11–13] but in each case, the decoupling of constituent subsurface phase components was not explored. This would have required a separate, simultaneously obtained topography data set in addition to the phase data, which is not afforded by contemporary quantitative phase imaging techniques.

In our investigation, intracellular information is extracted using simultaneously obtained sample phase and shear-force feedback topography data. After registration of the two images, the topography data is used to suppress surface information in the phase data to revealed enhanced subsurface information. Unlike confocal and optical coherence microscopy, the generated subsurface data is integrated rather than consisting of individual slices. This new technique however is much better suited for imaging individual cells than the aforementioned techniques, which are more appropriate for imaging thicker samples. Much of this research was focused on imaging relatively simple cells with a single major intracellular component, such as nucleated red blood cells. The procedure was initially applied to the imaging of fabricated structures with surface and subsurface features. In each case, both the shape and height of the subsurface structures were extracted with excellent reproducibility. It was also possible to determine the shape and size of the nuclei of fish red blood cells.

2. Quantitative phase imaging

A novel approach for quantitative phase imaging was utilized in this research. The details of the theory are published elsewhere [14]. The system was designed around a custom built near-field scanning optical microscope (NSOM) with a stabilized Mach-Zehnder interferometer.

#112155 - $15.00 USD Received 1 Jun 2009; revised 20 Jul 2009; accepted 11 Aug 2009; published 28 Sep 2009

Incorporation of the interferometric system was achieved by splicing an NSOM probe into one of the output arms of a bi-direction coupler as shown in Fig. 1(a). Since the interferometer is part fiber, stabilization against environmental noise is critical to phase determination. To achieve stabilization, a portion of the output arm of the coupler without the probe was tightly wrapped around a cylindrical piezo-electric transducer (PZT) modulated at 1 KHz. The detector D1 in Fig. 1(a) monitors the back-reflected signal from the output ends of the coupler. Stabilization was accomplished my maintaining the first harmonic component of this signal at zero, by active adjustment of the diameter of the PZT via a proportional integrating (PI) error signal. Environmentally induced optical path length changes were kept to within 2nm using this approach.

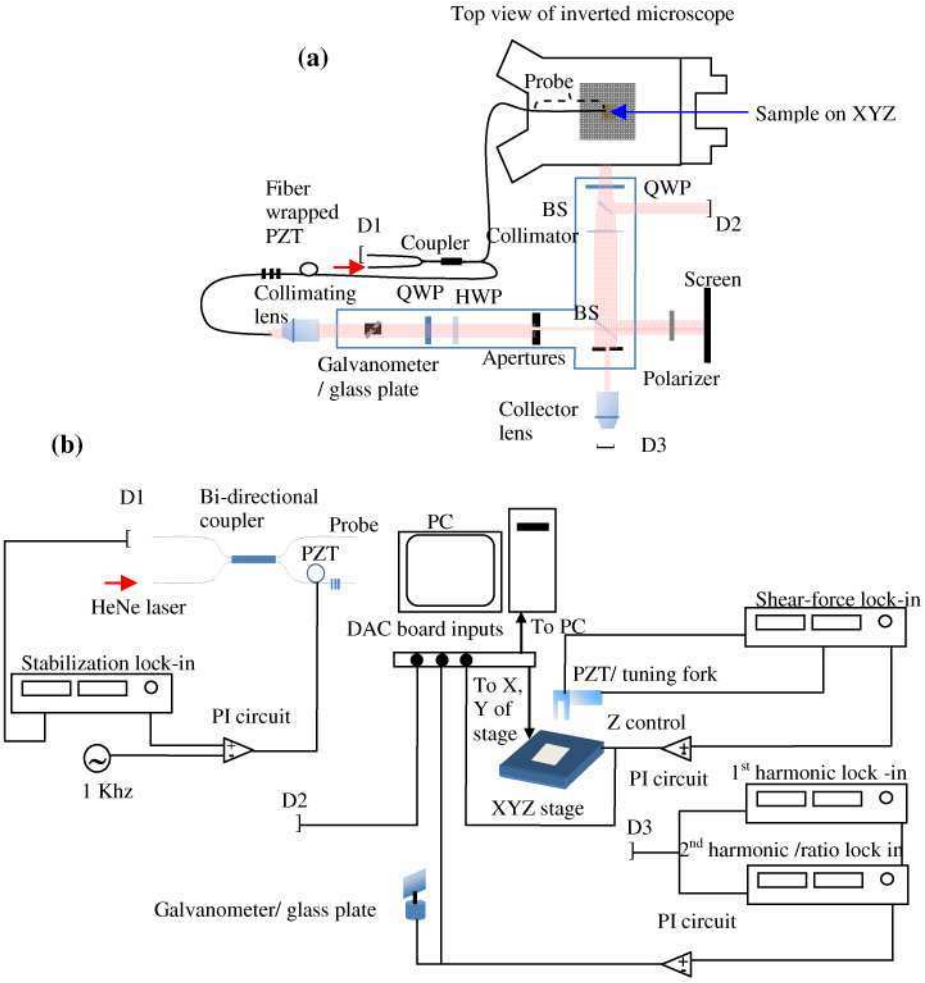

Fig. 1. Schematic (a) represents the optical setup. D1, D2, D3 photodiode detectors; BS, beam splitter; QWP, quarter wave plate; HWP, half wave plate. The screen, wave plates and polarizer are used for polarization adjustment of the sample and reference beams. Schematic (b) represents the electrical setup. PI circuits are used to compensate for environmental noise, Z adjustment of a precision XYZ stage and control of an angular displacement glass plate which is attached to a galvanometer.

As shown in Fig. 1(a), the sample sits on a three axis controlled precision stage. The X and Y controls were used to raster scan the sample relative to the spliced NSOM probe and the Z to maintain constant separation of the probe and sample during a scan. Sample phase was determined using the output signal at detector D3 which was modulated at 1 kHz (Ω) and

#112155 - $15.00 USD Received 1 Jun 2009; revised 20 Jul 2009; accepted 11 Aug 2009; published 28 Sep 2009

amplitude φ_o. From this signal, the first harmonic component $2\sqrt{(I_S I_R)}J_1(\varphi_o)\sin(\delta_e+\delta_s)\cos(\Omega t)$ and second harmonic component $2\sqrt{(I_S I_R)}J_2(\varphi_o)\cos(\delta_e + \delta_s)\cos(2\Omega t)$, were extracted and monitored by separate lock-in amplifiers, where I_S and I_R are the intensities of the signals from the sample and reference arms respectively. The environmental phase δ_e was kept at a constant as previously described and is given by $\delta_e = n\pi - \gamma_{pzt}$ where γ_{pzt} is the "error phase term" induced by adjusting the diameter of the fiber wrapped PZT. Prior to extraction of the sample phase δ_s, the first and second harmonic Bessel functions $J_1(\varphi_o)$ and $J_2(\varphi_o)$ respectively, must be equalized by adjustment of the modulation amplitude to the fiber wrapped PZT in Fig. 1(a). If this condition is met, then the ratio of the first harmonic voltage V_Ω and second harmonic voltage $V_{2\Omega}$ detected by the lock-in amplifiers is given by;

$$\frac{V_\Omega}{V_{2\Omega}} = \tan\left(\delta_e+\delta_S\right) \tag{1}$$

At this point, rather than calculating the sample phase directly from Eq. (1) which would require phase unwrapping, the ratio signal was used to adjust the position of an angular displacement plate attached to a precision galvanometer in the reference arm. The objective here was to actively compensate for feature-induced phase changes as the sample is raster scanned, by introducing corresponding changes in the reference arm such that the detected output phase is maintained at a constant. To accomplish this, the ratio signal given by Eq. (1) was maintained at zero by utilizing the error signal from a second PI circuit as shown in Fig. 1(b). This procedure allowed the output phase of the interferometer at each point in a sample scan to be maintained at a constant. Thus the angular position of the plate and correspondingly, the voltage applied to the galvanometer which controls the plate, are functions of the induced sample phase. Pre-calibration of the galvanometer allows for sample phase determination from an applied voltage. The calibration process involved using Eq. (1) to calculate the phase induced by the angular displacement plate as a function of applied voltage, without a sample in the sample arm. This procedure is an open loop process in contrast to sample phase determination which is closed loop. This phase extraction technique is unique in that it allows for real-time phase unwrapping. Although using a phase unwrapping algorithm is an option, this is often problematic for samples much thicker than the illumination wavelength [15]. From an experimental setup standpoint, this procedure is simpler than multi-wavelength unwrapping [16,17] and is effective over a much wider thickness range. Reliable unwrapping of thick samples is a prerequisite for the subsequent subsurface information extraction.

In our experimental setup, a precision three axis controlled stage was mounted on top of an Olympus X50 inverted optical microscope as shown in Fig. 1 (a). The microscope allows for NSOM probe positioning and sample examination prior to scanning. In the near-field scanning optical microscope, high spatial optical imaging is achieved by positioning and scanning a metal coated fiber probe with a subwavelength size aperture in a region which is extremely close to the surface of the sample [18]. While scanning in this region referred to as the near-field region, the emitted optical field from the tip interacts with an area of the sample which is approximately equal to the aperture size. However a probe/ sample distance regulation scheme is required to maintain constant separation and avoid catastrophic collision of the probe with the sample. In modern NSOMs, the most common method of achieving this is to employ a shear-force feedback system in which an NSOM probe attached to a dithered quartz tuning fork acts as a mechanical "pickup" for probe/sample interaction forces [19]. The phase between the signal generated by the tuning fork and that applied to the dithering piezo, varies as a function of the separation distance between the probe and sample. Therefore, the objective in this scheme is to maintain the phase difference between these two signals at a constant by employing a PI circuit to apply an error bias to the Z axis of the precision stage. In addition to height regulation, shear forced feedback topography data can be generated from this error signal. An intensity image is also simultaneously obtained from the signal which is transmitted through the sample and detected by detector D2 of Fig. 1(a). All signals in the

#112155 - $15.00 USD Received 1 Jun 2009; revised 20 Jul 2009; accepted 11 Aug 2009; published 28 Sep 2009

setup were monitored with photodiode detectors. Imaging processing was performed using proprietary Matlab code.

3. Subsurface imaging

During a scan, intensity, phase and surface topography data points are simultaneously obtained at predetermined time intervals. The latter image is used to extract the subsurface details from the phase data. Intensity line scans are useful in locating subsurface features for the purpose of probe positioning prior to scanning. Although a near-field setup is employed, the optical images are not near-field images due to the thicknesses of the imaged samples, which ranged from 1 to 3 microns. Consider a simple biological cell with a nucleus of thickness h and refractive index n_n as shown in Fig. 2. The height of the cell is given by H, the refractive index of the cytoplasm by n_c and the induced phase at points A and B by $\Delta\theta_A$ and $\Delta\theta_B$ respectively. The phase change $\Delta\theta_{BA}$ between points B and A is given by $\Delta\theta_{BA} = \Delta\theta_B - \Delta\theta_A$.

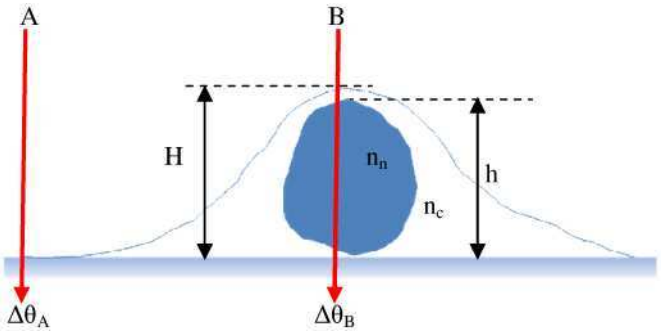

Fig. 2. The schematic shown represents a simple biological cell with a single prominent subsurface feature. The nucleus has a height h and protrudes through the cell membrane as is typical. The cell has an external height H.

It can be shown that the subsurface feature height is given by;

$$h = \frac{\lambda}{2\pi(n_n - n_c)}\left(\Delta\theta_{BA} - \frac{2\pi}{\lambda}H(n_c - 1)\right) \tag{2}$$

where λ is the illumination wavelength of 632.8 nm. The cell's thickness H is determined directly from the shear-force feedback topography data. This data contains information about the surface morphology and can be expressed as a phase change using the expression;

$$\Delta\theta'_{BA} = \frac{2\pi}{\lambda}H\left(n_c - 1\right) \tag{3}$$

Thus we can represent the subsurface feature height at any point (x, y) as;

$$h(x, y) = \frac{\lambda}{2\pi\Delta n(x,y)}\left(\Delta\theta_{BA}(x,y) - \Delta\theta'_{BA}(x,y)\right) \tag{4}$$

where Δn(x,y) is given by $n_n(x, y) - n_c(x, y)$. Thus the subsurface height at any point is proportional to the difference between the measured phase and the phase equivalence of the surface height at that point.

During the experimental setup, it is extremely difficult to position the probe exactly orthogonal to the plane of the substrate beneath. As such, there is a displacement between the shear-force and phase data because slightly different regions are accessed as shown in Fig. 3. The emitted field from the tip interacts with a sample region which depends on the tilt of the probe but the shear-force interaction occurs between the tip and the region directly below. Thus when the probe is above region A at a position (x, y), a topography value T(x, y) is

#112155 - $15.00 USD Received 1 Jun 2009; revised 20 Jul 2009; accepted 11 Aug 2009; published 28 Sep 2009

measured in addition to the phase value $P(x', y')$ at the nearby point (x', y'), instead of the phase P(x, y) at A. The displacement in the acquired data sets ranges from 200- 500nm in both directions. This is corrected using an image registration algorithm prior to image subtraction. The image subtraction procedure is analogous to the case of digital subtraction angiography in which a mask (topography data) is subtracted from a reference data set (phase data) [20]. Unless registration is perfect, a residue difference error results after image subtraction. This error was minimized by suppressing sharp peaks in the difference data.

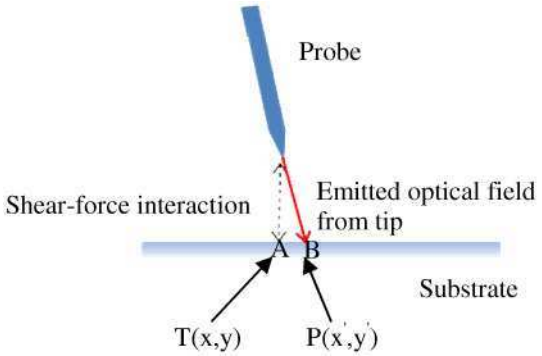

Fig. 3. The diagram depicts a typical orientation of the tip relative to the sample. The tilt of the probe is exaggerated to emphasize the displacement between the acquired phase and topography images.

4. Results

Both fabricated and biological samples were investigated as part of this research. The fabricated samples were designed with both surface and subsurface features. First a sample with subsurface features only was fabricated by etching trench patterns of various depths and widths onto a quartz glass substrate via reactive ion etching, followed by planarization of these surface features with SU8 photoresist. This was followed by the deposition of human red blood cells onto the planar layer, directly about the subsurface trenches. A schematic of a fabricated sample is shown in Fig. 4(a). The etched features ranged in depth from 0.15 to 1.5 microns and width from 1 to 10 microns. Figures 4 (b) and (c) illustrates the phase and topography scans respectively for a sample with a 10 microns wide, 0.5 microns tall, planarized trench. Approximately 6 microns of photoresist was required for complete planarization. The dotted white line in each image indicates the regions from which the line scans shown in (d) were obtained. The red plot of 4(d) corresponds to the phase line scan and the blue corresponds to the SFF. Figures 4(e) and (f) represent the intensity and extracted subsurface images respectively. It is observed that the phase image contains coupled surface and subsurface information, as is typically the case when imaging biological samples.

#112155 - $15.00 USD Received 1 Jun 2009; revised 20 Jul 2009; accepted 11 Aug 2009; published 28 Sep 2009

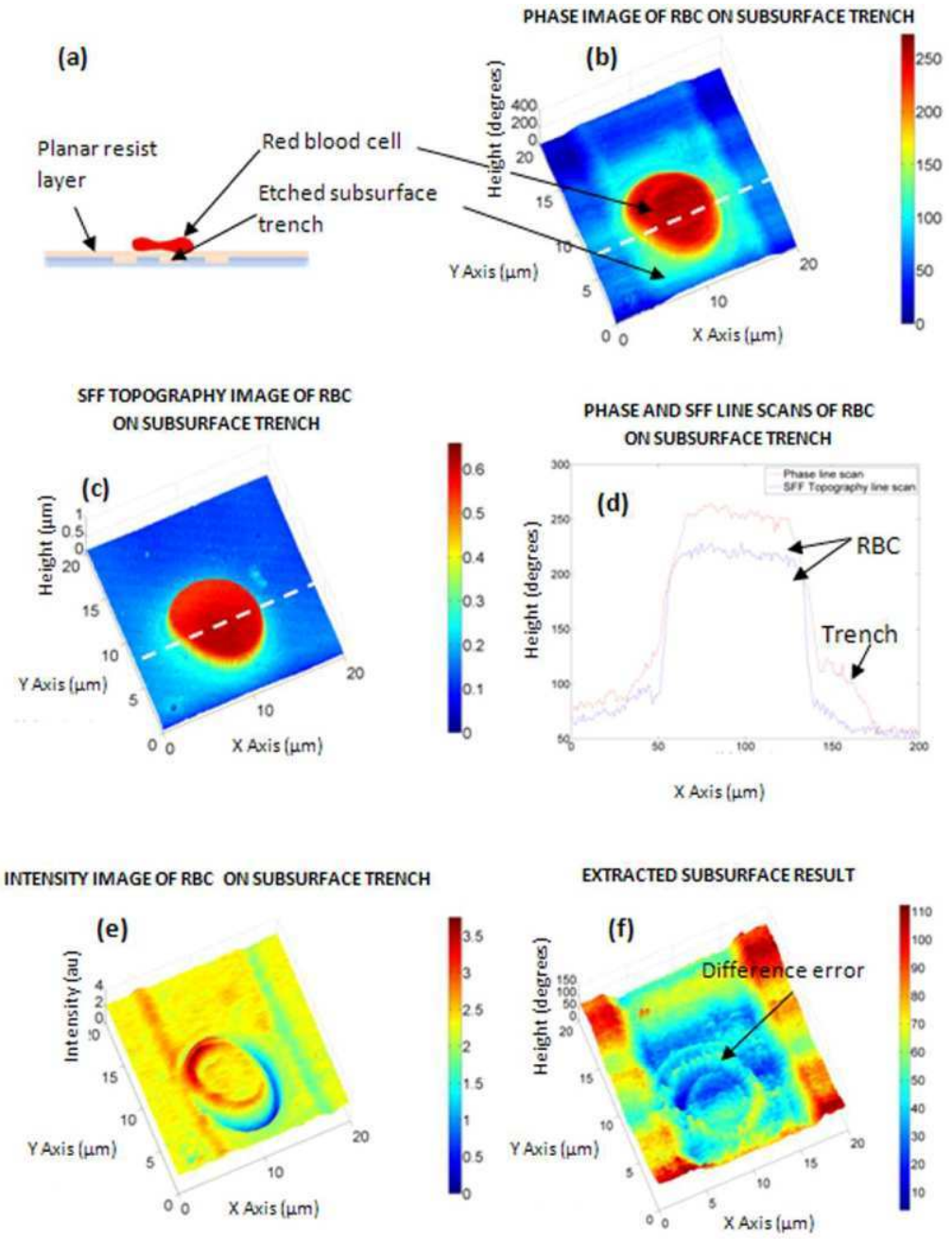

Fig. 4. A schematic of a fabricated sample with surface/ subsurface features is show in (a). Images (b) and (c) are phase and shear-force feedback (SFF) topography images respectively for a sample such as that shown in (a). The subsurface trench was 10 microns wide and 0.5 microns tall. The white dotted lines in (b) and (c) correspond to the regions from which the line scans shown in (d) were obtained. Image (e) is the intensity image of the sample while (f) represents the extracted subsurface trench. After subtraction and suppression of sharp peaks, a small difference error still remains.

The topography image however, depicts only the enucleated surface red blood cell but not the subsurface trench. This is readily confirmed by the line scans in (d). The intensity image highlights the edges in the sample but there is otherwise little contrast, although both the

#112155 - $15.00 USD Received 1 Jun 2009; revised 20 Jul 2009; accepted 11 Aug 2009; published 28 Sep 2009

surface red blood cell and the subsurface trench are clearly identified. It is important to note that the mere recognition of the presence of surface and subsurface components in the phase data is only possible after a comparison with the topography data or with prior knowledge about the surface morphology. It is possible to reliably separate these components after processing the phase and topography data which includes registration, subtraction and the suppression of difference errors. Although a small difference error is always present as shown in (f), it is usually possible to significantly reduce this undesired information.

Certain types of red blood cells such as those from amphibians and fishes are nucleated, as opposed to those from mammals which are usually enucleated. Humans in particular have discoid enucleated erythrocytes. In this investigation, the results from a human and fish red blood cell were compared. In each case, samples were prepared by smearing a tiny drop of blood onto a glass substrate and allowing the sample to air dry. In the case of the human erythrocytes, the phase and shear-force feedback topography images are essentially identical as seen in Figs. (5a) and (5b) respectively. The topography data was converted to phase data prior to registration and subtraction using Eq. (3). An average refractive index of 1.41 was assumed for the cell. The diameter of the cell was determined to be approximately 7 microns and the height was approximately 1.8 microns.

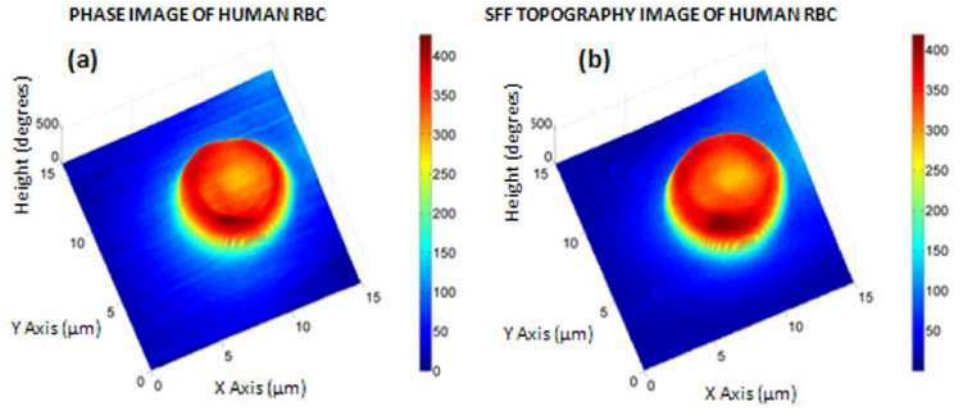

Fig. 5. Images (a) and (b) depict the phase and SFF topography images respectively of a human red blood cell. It is clear that there are no significant subsurface features present as the phase and SFF images closely agree.

After registration of the two data sets, corresponding line scans match up almost exactly in the x and y directions as seen in Fig. 6(a). The discoid shape is also apparent. Only the edges of the specimen are highlighted in 6(b) as expected given the homogenous nature of the cell in question. The registration process is never perfect and a difference error often results after subtraction of the two data sets. The subtraction result is expressed in image 6(c). This error can be suppressed by minimizing sharp peaks in the difference image. The result of applying a spike suppression algorithm is shown in 6(d). It is clear from this image that there are no significant subsurface features present, as expected. This is not necessarily the case as seen with a fish's red blood cell.

#112155 - $15.00 USD Received 1 Jun 2009; revised 20 Jul 2009; accepted 11 Aug 2009; published 28 Sep 2009

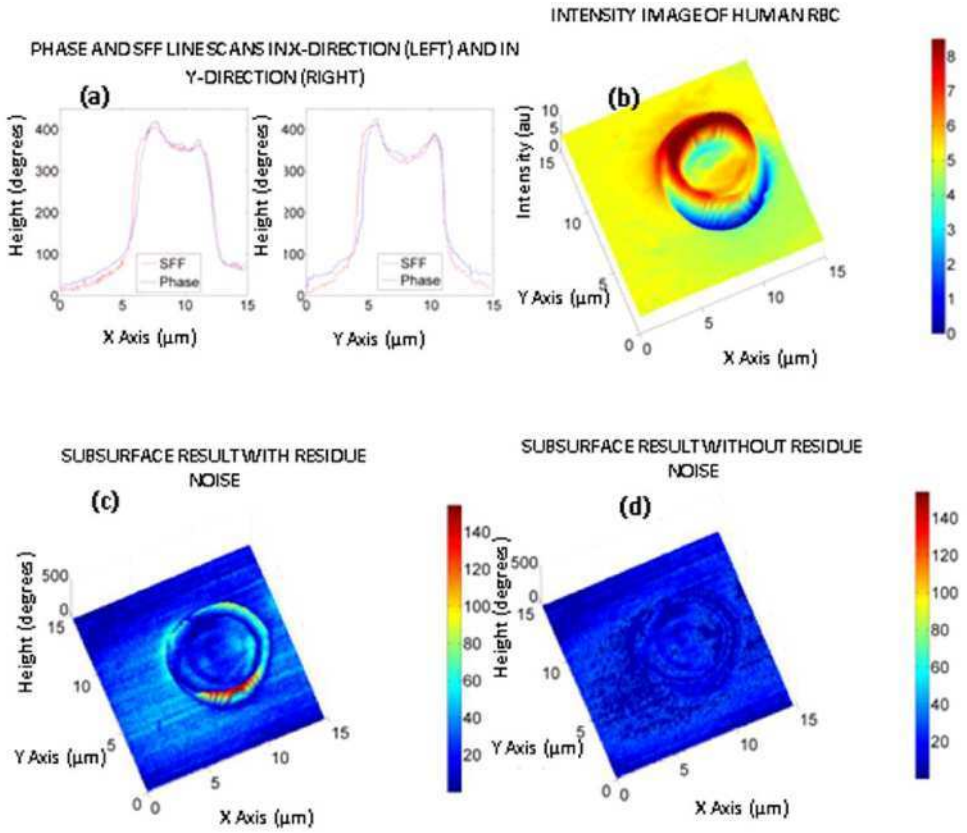

Fig. 6. Image (a) indicates line scans in the x direction (left) and y direction (right), at identical points in the phase and SFF images shown in 5 (a) and (b). Image (b) is an intensity image of the red blood cell. After registration and subtraction, a difference residue error results as shown in (c). Application of a spike suppression algorithm significantly reduces this error as seen in (d). From this image, it is conclusive that there are no significant subsurface features present.

This is a very different situation from the case of a fish's red blood cell. Erythrocytes from the silver dollar fish (Metynnis Argenteus) were examined as part of this investigation. Figures 7(a) and 7(b) represents phase and SFF images of a red blood cell from this species of fish. The nucleus protrudes through the surface and this is reflected as a bump at the center of the cell in both images. However, the highest point in the phase data corresponds to approximately 400 degrees whereas the highest point in the topography data corresponds to approximately 300 degrees. Thus it is apparent that there exists extra information in the phase which is not present in the topography data. The red blood cell was observed to have an elliptical shape with a short diameter or approximately 10 microns and a long diameter of 15 microns. By contrast, human red blood cells are smaller and possess a circular boundary. The extracted subsurface nucleus is shown in 7(c) and (d) in both 3D and 2D representations. The residue error is substantially suppressed in these images and the dominant features are clearly visible. The nucleus has an elliptical shape with long and short diameters of 7.5 and 5 microns respectively, and has a much rougher surface texture than that suggested by either the topography or phase data.

#112155 - $15.00 USD Received 1 Jun 2009; revised 20 Jul 2009; accepted 11 Aug 2009; published 28 Sep 2009

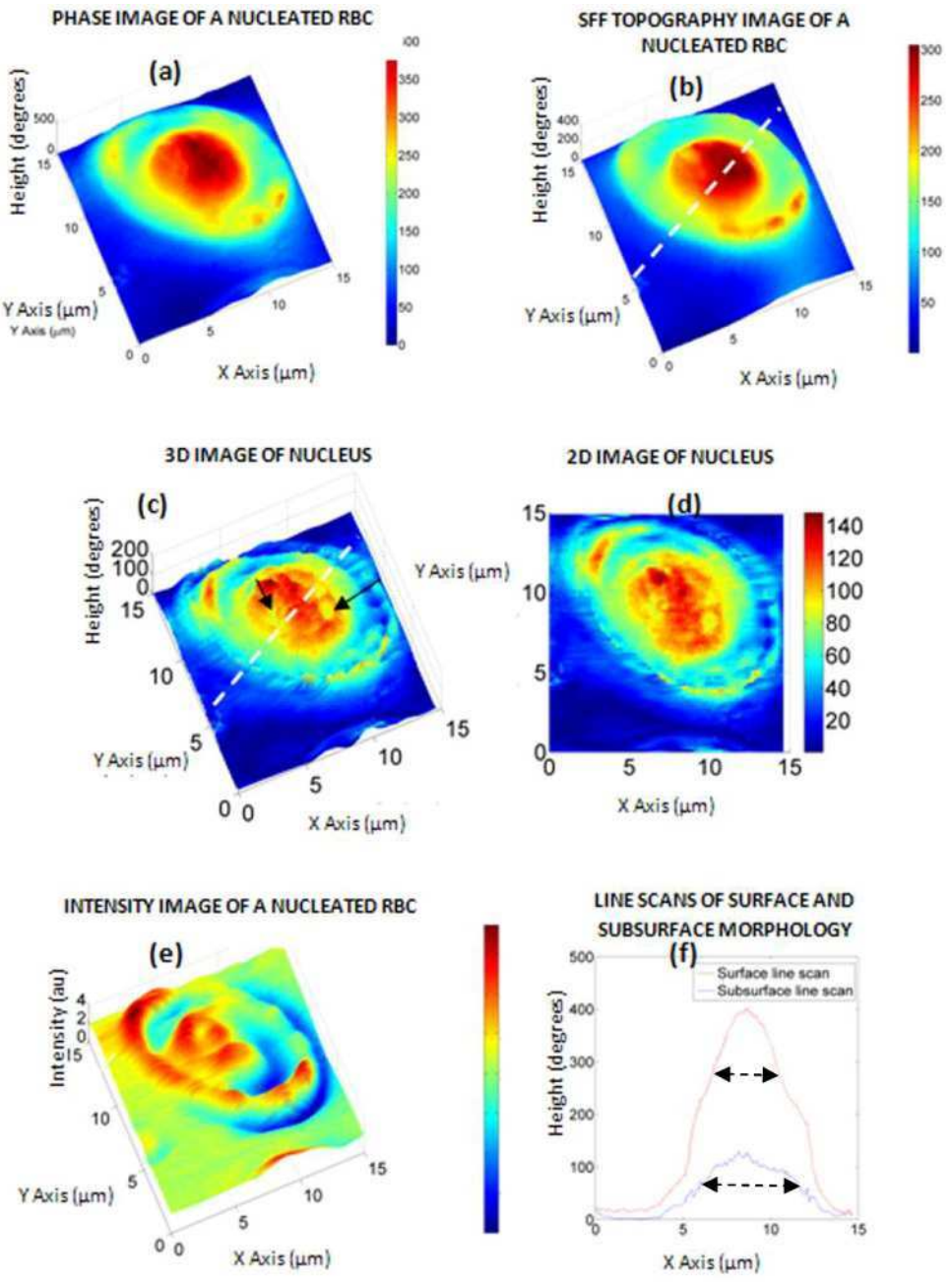

Fig. 7. Images (a) and (b) represents the phase and SFF images respectively of a fish's red blood cell. 3D and 2D representations of the extracted subsurface nucleus are shown in (c) and (d) respectively. The black arrows in (c) point to small pits on the surface of the nucleus. An intensity image of the cell in question is shown in (e). In image (f), the red plot is a line scan of the surface topography (across the dotted white line in (b)) and the blue line is a line scan of the subsurface nucleus (across the dotted white line in (c)). The black lines in (f) indicate the short diameter of the nucleus on the surface and subsurface line scans.

The black arrows in image (c) indentify tiny pits on the surface which is consistent with published descriptions [21]. Line scans of the surface and subsurface morphology are indicated by the red and blue plots respectively in 7(f). The short diameter of the nucleus as

#112155 - $15.00 USD Received 1 Jun 2009; revised 20 Jul 2009; accepted 11 Aug 2009; published 28 Sep 2009

measured from the SFF image was approximately 4.5 microns as compared to the diameter determined from the subsurface information which was about 5 microns. It is clear from these plots that the spatial extent of the nucleus is greater than that indicated by the rounded surface bump. Thus this procedure is more accurate for cellular volumetric analysis that an analysis of surface morphology information. If the refractive index of the nucleus is known, the volume of the nucleus can be easily calculated. This information was unavailable for the cell in question. Even if this information is unavailable, changes in the volume can be determined. This procedure thus has direct application to oncology studies of malignant cells and the investigation of intracellular parasites in their host, such as in the case of malaria. The aforementioned technique is suitable for the investigation of subsurface features as small as 1 micron wide which can be as much as 5 microns below the surface.

5. Conclusion

We have developed a simple procedure which allows for the examination of subsurface specimen/sample features. This has direct application to the imaging of constituent organelles of biological cells and intracellular parasites. Quantitative phase imaging by itself does not allow for direct subsurface imaging since the surface morphology and subsurface information are coupled. We have shown using a fabricated sample and biological cells that these two contributions can be effectively separated. In most of the results obtained, a residue error resulted from the subtraction process. This error can be significantly reduced by improving the registration algorithm. Currently, this procedure is best suited for cells in which the features of interest are away from the cell boundary. If this is not the case, it may be difficult to differentiate between the residue error and the feature.

The subsurface result of the fish's RBC depicted a nucleus with a well defined shape and distinct features. The structure is elliptical with notable pits and depressions. Given an average value for the nuclear refractive index, the height and subsequently volume, can be calculated. This would allow for the non invasive determination of nuclear volumetric changes of malignant cells, for example. Another possibility lies in tracking the growth and development of parasites inside a cell such as in the case of malaria infected cells. The potential for biological and non-biological refractometry studies is currently being investigated. A typical scans requires approximately 20 minutes but improving the temporal resolution of the system should allow for the investigation of slow dynamic biological processes. Current research is also directed at extending this procedure to the imaging of samples in a liquid environment.

Acknowledgement

We wish to thank Dr. Terrill W. Mayes for his invaluable assistance and advice throughout the course of this research.

#112155 - $15.00 USD Received 1 Jun 2009; revised 20 Jul 2009; accepted 11 Aug 2009; published 28 Sep 2009